Analysis of microtubule dynamic instability using a plus-end growth marker

Alexandre Matov[1], Kathryn Applegate[1], Praveen Kumar[2], Claudio Thoma[3], Wilhelm Krek[3], Gaudenz Danuser[1,4] & Torsten Wittmann[2]

Regulation of microtubule dynamics is essential for many cell biological processes and is likely to be variable between different subcellular regions. We describe a computational approach to analyze microtubule dynamics by detecting growing microtubule plus ends. Our algorithm tracked all EB1-EGFP comets visible in an image time-lapse sequence allowing the detection of spatial patterns of microtubule dynamics. We introduce spatiotemporal clustering of EB1-EGFP growth tracks to infer microtubule behaviors during phases of pause and shortening. We validated the algorithm by comparing the results to data for manually tracked, homogeneously labeled microtubules and by analyzing the effects of well-characterized inhibitors of microtubule polymerization dynamics. We used our method to analyze spatial variations of intracellular microtubule dynamics in migrating epithelial cells.

Microtubules are polymers of α/β-tubulin dimers that stochastically switch between phases of growth and shortening. These dynamics are generally reported by four parameters: the rates of growth and shortening and the frequencies of switching between these phases, referred to as catastrophes and rescues[1]. Conventional analysis of intracellular microtubule dynamics involves microinjection[2] or expression of fluorescently labeled tubulin[3] to homogenously label the microtubule network, and time-consuming, computer-assisted hand-tracking of individual microtubule ends over time[2,4]. Although computational modeling has improved the efficiency and reliability of this method[5], the analysis remains limited to microtubules near the cell periphery, where ends of labeled microtubules can be observed over sufficient periods of time. Substoichiometric labeling[6] allows microtubule observation deeper in the cell and could permit end tracking relative to the microtubule lattice, but the identification of microtubule ends and filaments in this context is an unresolved challenge; to date, only a few papers describe hand-measured data from limited numbers of microtubules[4,7].

An alternative strategy to visualize microtubule polymerization uses proteins that specifically recognize a structural property of growing microtubule plus ends, such as end-binding proteins 1

and 3 tagged with enhanced GFP (EB1-EGFP or EB3-EGFP)[8–10]. The exponential decay of available binding sites results in the characteristic comet-like fluorescence profiles of EGFP-tagged end-binding proteins ('comets'). Fast turnover[11] causes rapid loss of end-binding protein–associated fluorescence from non-polymerizing microtubule ends and rapid appearance of comets when microtubules start growing.
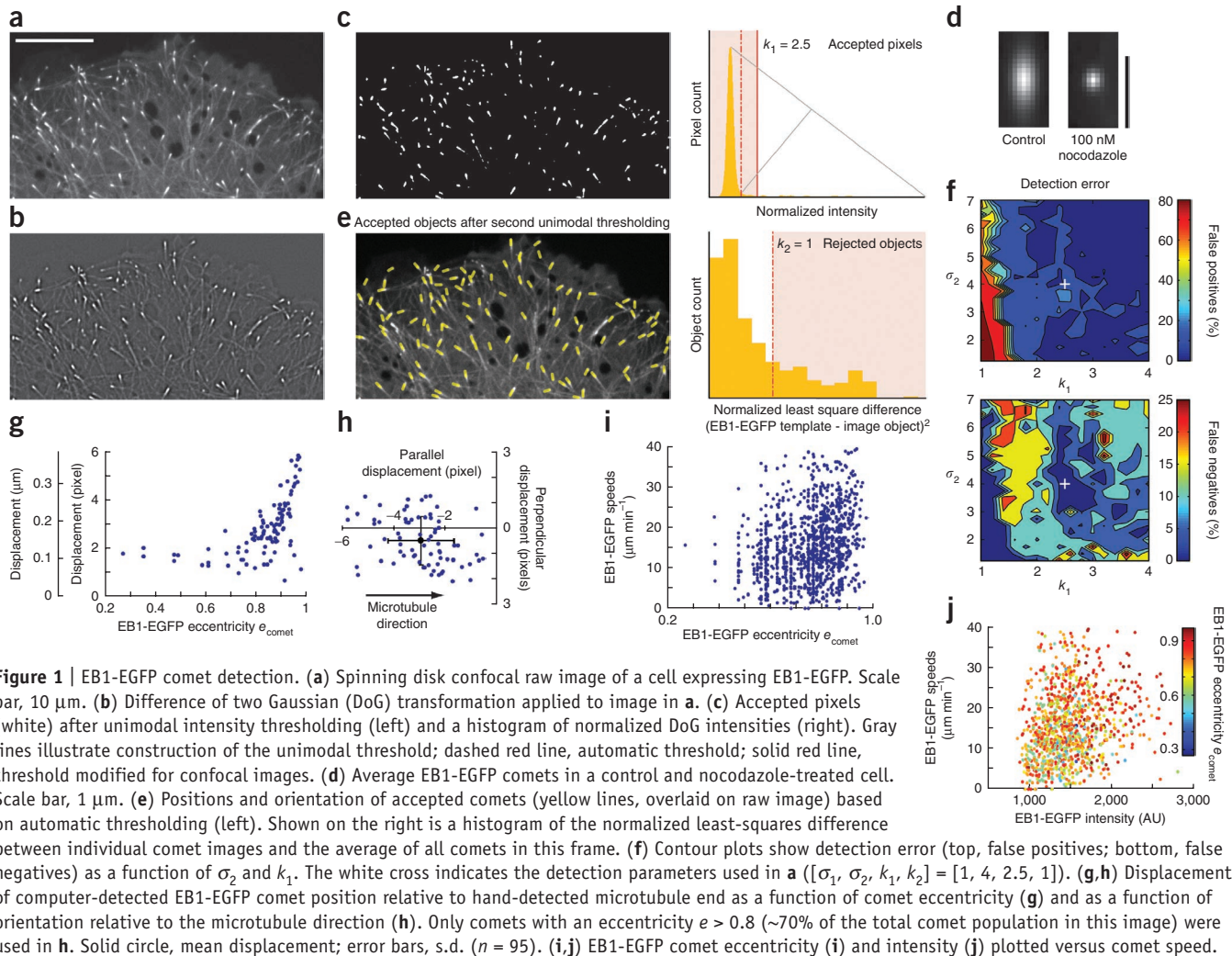
Here we describe a computational strategy to extract microtubule growth rates from EB1-EGFP time-lapse image sequences and introduce an approach to infer parameters of microtubule dynamics in pause and shortening phases without visible comets. We detected EB1 comets, tracked them to measure microtubule growth rates and spatiotemporally clustered EB1 growth tracks into more complete trajectories, which included inferred shortening and pause phases (**Supplementary Fig. 1**). This method allows analysis of a large population of intracellular microtubule ends in a spatially unbiased manner. Software packages implementing these algorithms are available as **Supplementary Software 1** and at http://lccb.hms.harvard.edu/software.html.

RESULTS

EB1-EGFP comet detection and tracking

To identify EB1-EGFP comets in each frame of a time-lapse sequence (**Fig. 1a**), we calculated the difference of two Gaussian transformations with s.d. σ_1 and σ_2 adjusted to enhance the band of image frequencies associated with EB1-EGFP comets (**Fig. 1b** and **Supplementary Note 1**). We used unimodal thresholding[12] to remove background pixels (**Supplementary Note 2** and **Fig. 1c**) and then generated individual objects likely corresponding to EB1 comets by connected component labeling of the thresholded difference of two Gaussians image (**Fig. 1c**). To discriminate against selected objects that are not true comets, we selected by template matching objects that conformed to the average shape of EB1-EGFP comets (**Supplementary Note 3** and **Fig. 1d**). For both thresholding steps, we introduced user-defined coefficients k_1 and k_2 to adjust the automatically detected threshold if required for specific imaging conditions. All adjustable parameters are summarized in **Supplementary Table 1**. Because

[1]Department of Cell Biology, The Scripps Research Institute, La Jolla, California, USA. [2]Department of Cell and Tissue Biology, University of California, San Francisco, California, USA. [3]Institute of Cell Biology, Swiss Federal Institute of Technology, Zurich, Switzerland. [4]Present address: Department of Cell Biology, Harvard Medical School, Boston, Massachusetts, USA. Correspondence should be addressed to G.D. (gaudenz_danuser@hms.harvard.edu) or T.W. (torsten.wittmann@ucsf.edu).

Figure 1 | EB1-EGFP comet detection. (**a**) Spinning disk confocal raw image of a cell expressing EB1-EGFP. Scale bar, 10 μm. (**b**) Difference of two Gaussian (DoG) transformation applied to image in **a**. (**c**) Accepted pixels (white) after unimodal intensity thresholding (left) and a histogram of normalized DoG intensities (right). Gray lines illustrate construction of the unimodal threshold; dashed red line, automatic threshold; solid red line, threshold modified for confocal images. (**d**) Average EB1-EGFP comets in a control and nocodazole-treated cell. Scale bar, 1 μm. (**e**) Positions and orientation of accepted comets (yellow lines, overlaid on raw image) based on automatic thresholding (left). Shown on the right is a histogram of the normalized least-squares difference between individual comet images and the average of all comets in this frame. (**f**) Contour plots show detection error (top, false positives; bottom, false negatives) as a function of σ_2 and k_1. The white cross indicates the detection parameters used in **a** ([σ_1, σ_2, k_1, k_2] = [1, 4, 2.5, 1]). (**g,h**) Displacement of computer-detected EB1-EGFP comet position relative to hand-detected microtubule end as a function of comet eccentricity (**g**) and as a function of orientation relative to the microtubule direction (**h**). Only comets with an eccentricity $e > 0.8$ (~70% of the total comet population in this image) were used in **h**. Solid circle, mean displacement; error bars, s.d. ($n = 95$). (**i,j**) EB1-EGFP comet eccentricity (**i**) and intensity (**j**) plotted versus comet speed.

we determined the average EB1 comet shape for each image, the detection was robust against variations throughout the time-lapse sequence, for example, during acute application of microtubule polymerization inhibitors that reduced the polymerization rate (**Fig. 1d**). Thus we obtained a list of EB1 comets for each frame (**Fig. 1e**), which included the position of the object centroid, the magnitude of EB1-EGFP comet eccentricity and the angular direction of its main axis.

To validate the detection algorithm, we compared the positions of ~120 hand-detected EB1-EGFP comets to automatically detected objects for different pairs of σ_2 and k_1 because these parameters are most sensitive to imaging conditions (**Fig. 1f**). Because the detection algorithm is sensitive to image-intensity variations at the size scale of EB1-EGFP comets, in confocal images in which a low EB1-EGFP signal was evident along the length of microtubules, we increased k_1 to $k_1 > 2$ to avoid a large number of false positive detections. In widefield images, however, in which EB1-EGFP along the microtubule lattice was obfuscated by out-of-focus light, the default pixel intensity threshold of $k_1 = 1$ worked robustly (**Supplementary Fig. 2**).

We quantified the detection error by the percentage of false positives, $100(1 - M/D)$, and the percentage of false negatives, $100(1 - M/G)$, where D is the number of computer-detected

comets, G is the number of hand-selected comets, and M is the number of matches between those two sets. We observed low correlation between σ_2 and false positive detections over most of the range of σ_2 values tested. Similarly, false negative detections did not follow a clear trend, but a shallow minimum was evident around $\sigma_2 = 4$ indicating that detection was most successful when σ_2 matched the length scale of EB1-EGFP comets (**Fig. 1f**). The detection performance was similar in widefield images. In agreement with its low correlation to σ_2 values, the performance was largely independent of the comet shape because the algorithm was applicable to the detection of other plus-end tracking proteins (**Supplementary Fig. 2**). Detection was also largely insensitive to simulated high-frequency pixel noise (**Supplementary Fig. 3**). We expect a small number of undetectable EB1-EGFP comets in every image because of proximity or overlap, which results in objects that do not pass the template matching of the detection algorithm. However, these events should not introduce a systematic error in the detected EB1-EGFP comet population. Moreover, temporary comet occlusion is largely compensated by subsequent growth-track clustering.

The elongated shape of EB1-EGFP comets implies that the comet centroid is systematically located behind the very tip of the microtubule. For growth-rate measurements this offset is

irrelevant as long as it remains constant over time. To assess the magnitude of potential temporal variation in the offset, we determined the difference between computationally defined EB1-EGFP comet positions and manually detected intensity maxima, which colocalized with the microtubule tip. As expected, the difference increased with comet eccentricity (**Fig. 1g**). Perpendicular to the microtubule direction the difference was small (0.49 ± 0.94 pixels) and below the accuracy of manual detection. For highly elongated comets, the difference was 2.95 ± 1.26 pixels along the direction of the microtubule (**Fig. 1h**); we estimated that the s.d. of this difference was sufficiently small to have minor impact on the analysis of microtubule growth (**Supplementary Note 4**). Because the elongation of the EB1-EGFP comet depends on the rate of microtubule growth[10], we expected a positive correlation between comet eccentricity and speed. Indeed, we found that the fastest comets had a high eccentricity, although the distribution also included many slower comets with equally high eccentricity (**Fig. 1i**). In contrast, no obvious correlation existed between eccentricity and EB1-EGFP peak intensity (**Fig. 1j**). Overall, this indicates complex kinetics of EB1 interactions with microtubule ends or fluctuations of microtubule end structures in cells.

We tracked detected EB1-EGFP comets using a Kalman filter–based multiobject tracking algorithm[13] (**Fig. 2**, **Supplementary Video 1** and **Supplementary Note 5**). As expected for random switching from growth to shortening, the track lifetime followed an exponential decay[14] with a mean lifetime $\tau = 3.6$ frames (**Fig. 2d**). Because the number of tracks with a lifetime of two frames was higher than expected, we suspected that a substantial subpopulation of very short tracks resulted from detection or tracking errors. Analysis of the variance of the growth rate histogram as a function of minimal lifetime also indicated a larger s.d. for short tracks (**Fig. 2e**). Thus, subsequent analysis only included growth tracks with a lifetime of four frames and greater. To evaluate the combined performance of the detection and tracking algorithms, we compared computer-generated tracks with simulated differences in spatial (**Supplementary Fig. 4**) and temporal resolution (**Supplementary Fig. 5**). We found that the algorithm performed robustly at magnifications that satisfy the Nyquist sampling criterion (effective pixel size of <100 nm), and that a temporal sampling of one to two frames s^{-1} was sufficient to achieve good track reconstruction of microtubule growth.

EB1-EGFP growth-track-cluster assignment

Microtubules are stiff[15], and over the short time intervals used to observe microtubule polymerization dynamics they translocate little. As a result, microtubule shortening, rescues and pauses predominantly occur along the path defined earlier by the growing microtubule end. Thus, time-shifted, nearly parallel EB1-EGFP tracks with considerable spatial overlap have a high probability of belonging to the same microtubule. To detect events of microtubule shortening and pausing in addition to the microtubule growth directly visible in EB1-EGFP sequences and to infer parameters of their associated dynamics, we developed a computational scheme to cluster tracks that fulfill defined geometrical and temporal constraints based on a priori assumptions about intracellular microtubule behavior (**Fig. 3a**).

Given an EB1-EGFP growth track terminating at time t, we considered all track initiations in the interval $[t + 1, t + T_{max}]$ in cones
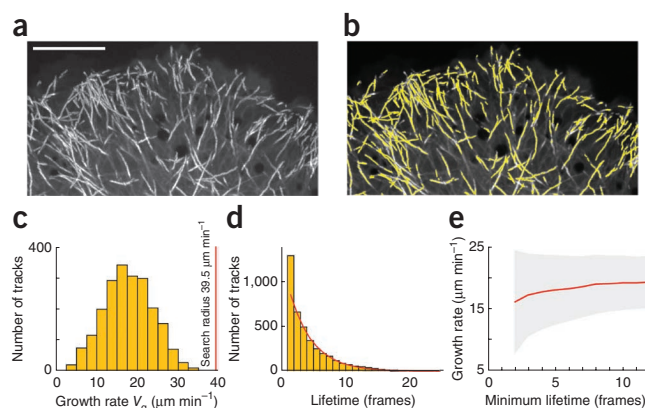
Figure 2 | EB1-EGFP object tracking. (**a**) Maximum intensity projection of EB1-EGFP time-lapse sequence (75 frames, 0.4 s frame^{-1}). Growing microtubule ends appear as bright tracks. Scale bar, 10 μm. (**b**) Computer-generated growth tracks (yellow) with a minimum lifetime of four frames. (**c**) Histogram of growth velocities. Red line indicates the maximum search radius. (**d**) Histogram of growth track lifetimes. Red line is the least-squares fit of a single exponential decay excluding the first data point. (**e**) Mean growth rates as a function of minimum growth track lifetime. Gray area, s.d.

with a forward opening angle $\varphi = \pm45°$ and a backward opening angle $\rho = \pm10°$ as candidate links. These links could potentially represent a continuation of the terminated growth phase after pausing or temporarily occluded growth (forward link) or shortening (backward link). The narrow backward cone reflects the tendency of microtubules to shorten along the preceding growth track[4]. For each candidate link we then calculated the maximal allowable distance for forward gaps (C_{fwd}) and backward gaps (C_{bwd}) as

$$C_{fwd} = V_{max} \min(\Delta t_{gap}, \sqrt{T_{max}}) \quad \text{and} \tag{1}$$

$$C_{bwd} = \min(\gamma V_{max} \Delta t_{gap}, V_{med} T_{max}). \tag{2}$$

V_{max} represents the 95th percentile of the speed distribution from all participating growth tracks, and Δt_{gap} is the time between termination and initiation of the two candidate tracks. Equation 1 assumes that short time gaps mainly result from temporary occlusion of growing microtubule ends owing to noise, overlap or out-of-focus motion, where the comet reappears at a distance proportional to the growth rate and Δt_{gap}. Long time gaps more likely represent bona fide pauses. During such pauses a microtubule end undergoes a random walk of short growth and shortening events, and the comet reappears at a distance proportional to the square root of time points without a detectable EB1-EGFP comet. In equation 2, γ takes into account that microtubule shortening is generally faster than growth[3,4]. $V_{med} T_{max}$, where V_{med} is the median of the growth track speed distribution and T_{max} is the maximum time window for linking, safeguards against the combinatorial explosion of candidate links in dense EB1 comet fields. Furthermore, we considered candidate links only when the directional change $\alpha_{i,j}$ between the two associated tracks was less than $\alpha_{max} = 60°$ (**Fig. 3b**) because microtubules rarely bend more than 60° over short distances[16].

From the set of candidate links that fulfilled the distance and angular criteria, we then selected the largest possible subset of

Figure 3 | EB1-EGFP growth-track clustering.
(**a**) Schematic of growth-track clustering. Green and red cones, spatiotemporal search space for candidate links to subsequent growth tracks at the end of a terminating growth track. Gray tracks with an initiation point inside a cone indicate tracks not selected for linking by the clustering algorithm; gray tracks with an initiation point outside any cone do not participate in the clustering. v_g, growth rate derived from EB1-EGFP tracks; v_{fwd} and v_{bwd}, inferred velocities of forward and backward gaps, respectively; t_x defines the time point of initiation or termination of a growth track. (**b**) Variables defining the cost of a candidate link between growth tracks. (**c,d**) Overlay of forward gaps (**c**) and backward gaps (**d**) on a maximum intensity projection of EB1-EGFP time-lapse sequence (97 frames, 0.6 s frame^{-1}). Blue, slow gaps; red, fast gaps. Insets, histograms of forward (**c**) and backward (**d**) gap speeds and unimodal thresholds to reject fast (**c**) and slow (**d**) gaps. (**e**) Image of a cell expressing mCherry-tubulin and EB1-EGFP. Boxes indicate image regions used for validation. Scale bar, 10 μm. (**f**) Hand-tracking (left) of 19 microtubules in region 1 in **e**. Periods of growth (green), shortening (red) and pauses (blue) are shown. Hand-tracked (green) and computer-tracked (yellow) growth is shown in the middle. Hand-tracked shortening overlaid on the EB1-EGFP maximum intensity projection of the entire sequence (right). (**g**) Track clusters obtained by two different settings for the cone openings. Color coding for lines, circles (growth track start) and asterisks (growth track and gap ends) is as described in **a**.
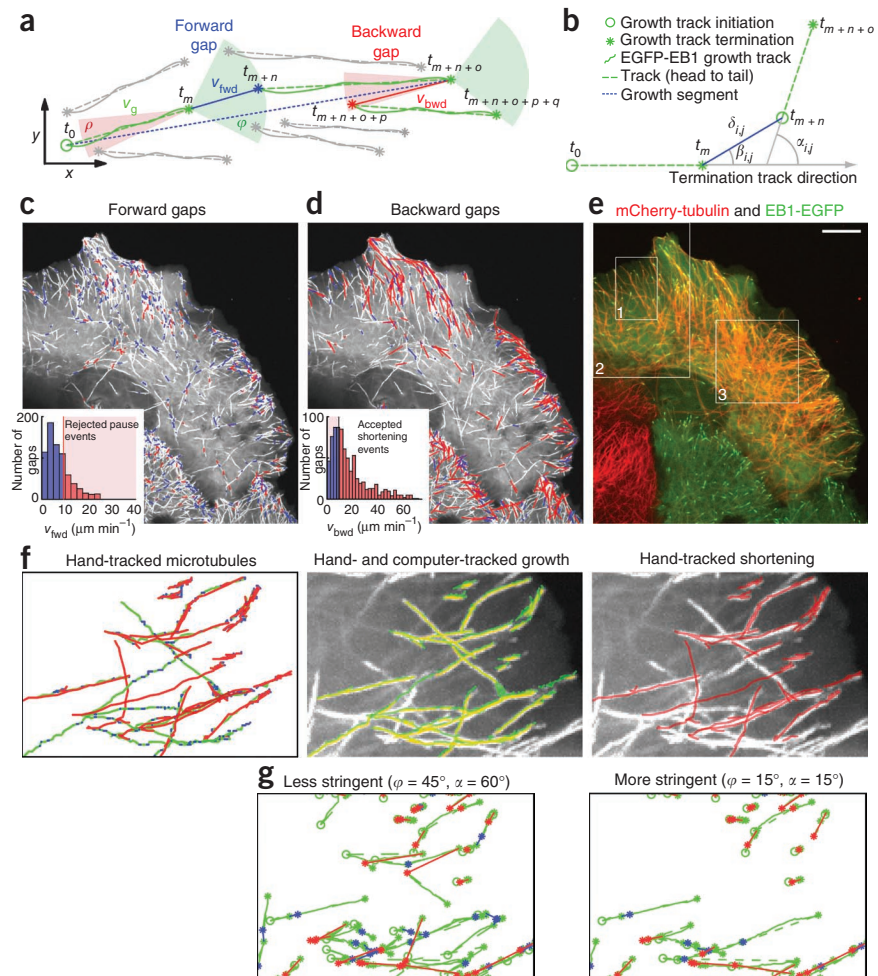
links with overall minimal cost using linear assignment[17,18]. The cost for an individual candidate link $c_{i,j}$ was defined as

$$c_{i,j} = \delta_{i,j} \left(\|\cos(\alpha_{i,j})\| - \|\cos(\beta_{i,j})\| \right), \qquad (3)$$

which gives preference to pairs of tracks in close proximity ($\delta_{i,j}$), with a low bending angle ($\alpha_{i,j}$), and with small transversal shifts ($\beta_{i,j}$). Although the methods currently used may generate some false positive links, the selection is fairly robust because all tracks compete for links simultaneously. In a typical EB1-EGFP time-lapse sequence, each growth track termination associated with ~200 candidate links that fulfilled the temporal (T_{max}) and angular criteria (φ, ρ and α_{max}). Applying the distance cutoffs (C_{fwd} and C_{bwd}) reduced this to an average of three competing track initiations. As expected, the majority of links were positioned in the cell periphery where microtubules more frequently switch between growth and shortening (**Fig. 3c,d**).

Forward gaps during which EB1-EGFP comets are invisible could be due to periods of pause or very slow growth during which the EB1-EGFP signal becomes too dim to be detected, or could be due to regularly growing EB1-EGFP comets that are temporarily out of focus. We therefore calculated the forward gap speed v_{fwd} as the distance between the last point in the terminating track and the first point in the linked growth track divided by the gap duration (**Fig. 3a,c**). Typically, less than 15%

of the forward gaps had a speed larger than the slowest 30% of the growth tracks. This indicated that most forward gaps represented true microtubule pausing. We expected a small forward translocation even for true pause events because of the latency of detectable EB1-EGFP comet formation at the end of a newly growing microtubule (**Supplementary Note 6**). Similar to forward gaps, backward gaps contain information about microtubule shortening events, and as above we calculated a backward gap speed v_{bwd} (**Fig. 3d**). Of note, the histograms of both v_{fwd} and v_{bwd} sharply decayed toward the last bin below the maximally allowable velocity. This is an indication that the distance cutoffs in equations 1 and 2 were set sufficiently large to capture the majority of clusters of aligned growth tracks (**Fig. 3c,d**).

Algorithm validation
To evaluate the performance of growth-track clustering, we recorded dual-wavelength time-lapse sequences of cells expressing both EB1-EGFP and monomeric (m)Cherry-tubulin (**Fig. 3e**). Because mCherry-labeled microtubules were too dense in the cell interior to directly observe dynamic ends (**Supplementary Fig. 6**), we hand-tracked 19 microtubules in a peripheral cell region in which microtubule ends were clearly visible (**Fig. 3f** and **Supplementary Video 2**). Detection and tracking of EB1-EGFP comets was accurate as indicated by the overlap of hand- and computer-tracked growth (**Fig. 3f** and **Supplementary Video 3**).

Table 1 | Comparison between computer-inferred and hand-tracked microtubule dynamics

	Growth (µm min⁻¹)	Shortening (µm min⁻¹)	Pause (µm min⁻¹)	Pause duration (s)
Computer-inferred (raw)	16.8 ± 7.4 n = 2,799	17.6 ± 14.7 n = 775	7.2 ± 5.2 n = 704	6.9
Computer-inferred (corrected)	18.7 ± 7.4 n = 2,351	24.4 ± 14.3 n = 499	4.6 ± 2.4 n = 517	8.2
Hand-tracked (raw, segment by segment)	21.7 ± 8.4 n = 582	39.4 ± 22.6 n = 283		
Hand-tracked (corrected, head to tail)	19.1 ± 7.4 n = 122	24.9 ± 12.8 n = 70	4.3 ± 3.4 n = 105	3.0

Both computer-inferred rate measurements using EB1-EGFP comet tracking and cluster analysis and hand-tracked microtubule trajectories of homogeneously labeled microtubules were adjusted to make the underlying assumptions more comparable. Pauses per microtubule are not initially defined in segment-by-segment hand-tracked datasets. Values are means ± s.d.

Although clustered growth tracks and hand-tracked microtubule trajectories were similar, qualitative comparison showed that the algorithm missed many shortening events (**Fig. 3g**). We expected this because the clustering algorithm cannot detect shortening that is not preceded or followed by a growth track within the distance and angle criteria. However, a high percentage of false negatives is acceptable as long as the population of microtubules analyzed is sufficiently large and unbiased to provide a representative readout of overall microtubule dynamics. To quantitatively test this, we compared hand-tracked rates of growth, pause and shortening, and pause durations to those obtained by computational analysis. The definition of growth, pause and shrinkage events by hand-tracking relies on user-defined judgment as to when a microtubule undergoes a change in velocity. The definition of these events by growth-track clustering relies on the detection of EB1-EGFP comets as molecular markers of microtubule growth. Therefore, before a comparison of hand- and computer-tracking, we had to correct the hand-tracked measurements to account for the differences in assumptions (**Supplementary Note 7**).

Even after these corrections, hand-tracked growth and shortening rates were substantially higher than the computer-inferred rates (**Table 1**). This deviation originated in the fundamentally different definitions of growth, pause and shortening events in tracking by hand and computer-tracking. At the high temporal resolution used for EB1-EGFP comet tracking, a subset of computer-tracked growth events were slower than the accuracy that can be achieved by manual detection. In hand-tracked trajectories such events would be classified as pauses. Similarly, computer-inferred backward gaps contained very slow events that would be classified as pauses in hand-tracked trajectories, in addition to phases of true microtubule shortening. We determined a threshold for a computer-generated forward or backward gap to be accepted as a pause or shortening event, respectively, by analysis of the forward gap velocity distribution, which includes both bona fide pauses and gaps owing to unobserved growth events (**Supplementary Note 8**). This filtering resulted in excellent agreement between computer-inferred and hand-tracked growth and shortening rates (**Table 1**). Thus, although comparisons between computational analysis and hand-tracking cannot be made directly, reasonable assumptions about the limitations of both methods confirmed that the growth and shortening rates we inferred are representative of microtubule polymerization dynamics. A discrepancy between computer-inferred and hand-tracked

pause durations remained (**Table 1**), likely owing to the latency of EB1-EGFP comet formation and disappearance (**Supplementary Note 6**). Thus, pause durations inferred by the clustering algorithm were not directly comparable to hand-tracking of homogenously labeled microtubules. Similarly, because shortening events interrupted by pauses will be combined into a single phase, the computer-inferred v_{bwd} is not a direct measure of the microtubule depolymerization rate. Nevertheless, we expect that molecular conditions that change microtubule polymerization dynamics will result in relative changes of these computer-inferred parameters.

The clustering algorithm also generated erroneous connections between growth tracks not belonging to the same microtubule. To quantify the frequency of such events, we overlaid clustered trajectories generated with two different stringencies onto mCherry-tubulin and EB1-EGFP channels (**Supplementary Videos 4–6**) and verified computer-assigned growth, pause and shortening phases, as well as catastrophes and rescues. In the region analyzed (**Fig. 3e**), the software accumulated 475 microtubule growth tracks lasting at least four frames. At the less stringent parameter set ($\phi = 45°$, $\alpha = 60°$) 329 tracks clustered into 118 trajectories with an average lifetime of 17 s. For the more stringent parameters ($\phi = 15°$, $\alpha = 15°$) 226 tracks clustered into 91 trajectories with a 14 s average lifetime. Only 8% of the trajectories were identical between the two analyses, indicating the sensitivity of the clustering process in selecting viable track connections (**Fig. 3g**). Because of the high microtubule density, about half of the computer-assigned events could not be observed clearly. However, if we only considered events that we could visually confirm as true or false, our algorithm showed good performance (**Supplementary Table 2**). As expected, the high stringency parameter set was more accurate, and with both parameter sets, the software more robustly connected microtubule growth tracks interrupted by pause rather than shortening events. However, the better performance at high stringency came at the expense of less data, which bears the risk that some of the heterogeneity of microtubule behavior is lost.

We next tested whether the computational analysis detected well-characterized responses to pharmacological microtubule dynamics inhibitors. At low concentrations, nocodazole reduces both growth and shortening rates and increases the time microtubules spend in pause[19], and we detected statistically significant effects ($P < 0.05$) on these parameters with as little as 10 nM nocodazole (**Fig. 4a–c**). Similarly, at low taxol concentrations we reproduced published effects[20] (**Fig. 4d–f**). This demonstrated that our computational analysis was sufficiently sensitive to detect expected differences in microtubule polymerization dynamics. The results obtained with two different clustering parameter sets were similar, indicating that the number of false positives was sufficiently low so as to not bias correctly clustered microtubule growth tracks.

Effects of microtubule acetylation and spatial cues
Armed with our new software tool, we examined two long-standing questions in the field: first, we tested whether tubulin acetylation[21]
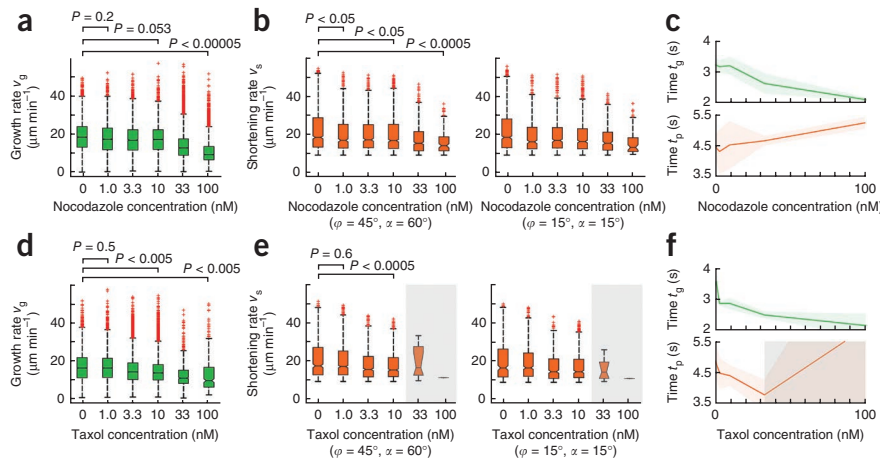
Figure 4 | Effects of microtubule inhibitors. (**a**–**f**) Growth rates (**a**,**d**), inferred shortening rates using two different sets of clustering parameters as indicated (**b**,**e**) and durations spent in growth and pause (**c**,**f**) as a function of nocodazole (**a**–**c**) and taxol (**d**–**f**) concentration. Box plots indicate the 25th percentile (bottom boundary), median (middle line), 75th percentile (top boundary), nearest observations within 1.5 times the interquartile range (whiskers) and outliers (red crosses). The shaded areas in **c** and **f** indicate s.d., and the gray area in the taxol-treatment experiment indicates unreliable results owing to very few growing microtubules (<5–10% of control), which resulted in low clustering efficiency. Data were pooled from three cells for both experiments; distributions comprise > 3,000 measurements for each concentration except those in the gray areas. Significance of the difference between concentrations was determined by a permutation *t*-test.

alters microtubule polymerization dynamics. We treated cells with trichostatin A, a broad-specificity histone deacetylase inhibitor that inhibits the tubulin-specific deacetylase HDAC6 (ref. 22) (**Fig. 5a**). We could not detect significant ($P > 0.1$) differences in microtubule dynamics in cells treated with trichostatin A alone. However, in cells simultaneously incubated with 50 nM nocodazole, the inferred shortening rate in trichostatin A–treated cells decreased significantly ($P < 0.05$) (**Fig. 5b**). This indicates that tubulin acetylation may protect microtubules from nocodazole-induced depolymerization.

Second, we examined spatial gradients of intracellular microtubule dynamics. We and others have reported that microtubules grow more slowly at the cell edge[23,24]. We thus determined the distance from the cell edge at which the difference in the median microtubule growth rate between the edge and interior microtubule populations was greatest. In three cells analyzed, this distance varied between 3.7 μm and 6.4 μm (**Fig. 5c,d**). The median growth rate in the cell body was 19.7–22.7 μm min^{-1} compared to 16.6–17.1 μm min^{-1} closer to the cell edge. The inferred shortening rate was not significantly different ($P = 0.71$) (**Fig. 5e**), but at the cell edge a larger fraction of the links between growth tracks were backward links (44–60% in comparison to 35–43% in the cell interior), consistent with the observation that peripheral microtubules more frequently switch between growth and shortening[23,25].

We recently reported that GSK3β inactivation may be required for spatial microtubule dynamics regulation in migrating epithelial cells[24] but had not observed differences in the spatial gradient of growth rates between control cells and cells expressing constitutively active GSK3β(S9A). Here we first confirmed this result using our new method for identifying spatial gradients in microtubule dynamics (**Fig. 5f**). Our clustering algorithm then revealed a large decrease in catastrophe probability at the cell edge and a decrease in the percentage of time microtubules spent in the shortening phase

(**Fig. 5g–i**). This demonstrates that GSK3β regulated specific aspects of microtubule polymerization dynamics and is consistent with the hypothesis that GSK3β inactivation increases cell edge microtubule interactions with the cortical cytoskeleton[24]. The clustering algorithm detected these differences even though growth and shortening rates at the cell edge of control and GSK3β(S9A)-expressing cells were not significantly different ($P > 0.05$).

DISCUSSION

We present a framework for the analysis of intracellular microtubule polymerization dynamics based on automatic tracking of a microtubule plus end marker such as EB1-EGFP and geometric clustering of growth tracks. Because we never observed growing microtubules without associated EB1, and no condition has been reported that selectively removes EB1 from a subset of growing microtubule ends, EB1-EGFP is a faithful reporter of the entire intracellular microtubule population. As EB1-EGFP overexpression may influence microtubule dynamics by enhancing growth rates[26], stabilizing microtubules against catastrophes[27] or by disrupting the localization of other plus end–tracking proteins[28], it is important that our algorithm allows comet detection at low expression levels. The algorithm may be used with other plus-end markers such as EGFP-CLIP-170, allowing independent experimental validation. In addition, because a universal EB1-binding motif has been identified[29], artificial plus end trackers will likely be available soon that only minimally affect microtubule dynamics.

Because EB1-EGFP only labels growing microtubules, microtubule behavior has to be interpolated when microtubules stop growing. We introduced several assumptions about the average behavior of microtubules, including maximum rates, allowed angles for direction changes and the observation that microtubules shorten along the track previously defined by the growing end, to link growth tracks probably belonging to the same microtubule. We designed the linking to prefer exclusion of uncertain events. Thus, our algorithm produces a relatively low number of false positives but a high number of false negatives. We estimate that only 20–30% of pause and shortening events are captured.

Although we extensively validated our clustering algorithm by visual comparison with time-lapse sequences that included homogeneously labeled microtubules, we currently have no formal way to quantify the frequency of clustering errors. This is an important caveat because different imaging conditions or different intracellular densities of growing microtubule ends may affect clustering efficiency. Thus, when using this method, thorough experimental controls must be performed to avoid the propagation of systematic errors (**Supplementary Note 9**). It is also important to note that measurements inferred by cluster analysis are not directly comparable to traditionally reported parameters of microtubule dynamics because the assumptions underlying both analysis methods are fundamentally different.
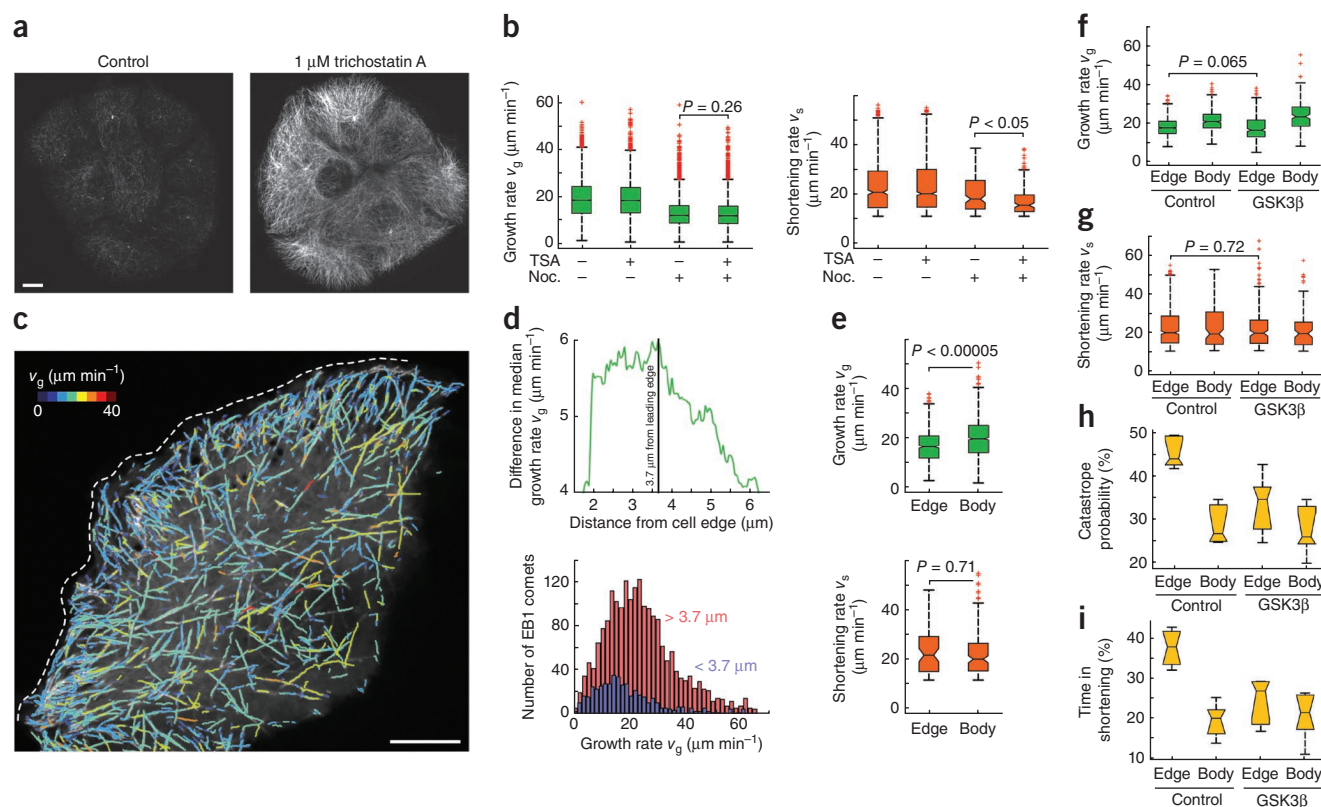
Figure 5 | Effects of tubulin acetylation and spatiotemporal microtubule regulation in migrating cells. (**a**) Immunofluorescence staining of acetylated microtubules in control and trichostatin A–treated cells. Scale bar, 10 μm. (**b**) Growth and shortening rates in the presence of the indicated compounds. Data were pooled from three cells (each distribution comprises >3,000 measurements) and tested by permutation t-test. (**c**) Computed growth tracks overlaid on a maximum intensity projection of an EB1-EGFP time-lapse sequence at the edge of a cell monolayer (77 frames, 0.4 s frame^{-1}). Growth tracks are color-coded by growth rate as indicated; the dashed white line marks the leading edge. Scale bar, 10 μm. (**d**) Difference in median growth rate of microtubule populations in the cell body and cell edge as a function of distance from the edge (top). The plot below shows the regionally separated histograms of growth rates. (**e**) Growth and inferred shortening rates in the cell body and at the cell edge. (**f**–**i**) Growth rates (**f**), inferred shortening rates (**g**), catastrophe probability (**h**; estimated as the fraction of backward links in the total population of links), and the time spent shortening, in regions of the cell edge compared to the cell body in control and GSK3β(S9A)-expressing cells (**i**). In **e**–**g** data were pooled from six cells (distributions comprise >3,000 measurements) and tested by permutation t-test.

For example, terminal shortening cannot be detected by our approach, and backward gaps may include pauses and short growth phases that do not produce a detectable EB1-EGFP comet. Nevertheless, our data showed that many growing microtubule ends measured throughout the cell reveal robust and spatially differentiated variations in microtubule polymerization behavior between experimental conditions. Our approach will thus complement and enhance conventional analysis, which typically reports the dynamics of very few microtubules tracked at the cell edge.

There is no mathematical reason precluding the adaptation of our approach to the analysis of microtubule dynamics in more physiological three-dimensional cell culture systems. In fact, the generalization of tracking and clustering has already been demonstrated in a study of kinetochore dynamics in mitotic spindles[30]. Detection of highly eccentric EB1-EGFP comets in three dimensions will be more complex because of the unequal optical resolution in lateral and axial directions. Thus, the comet shape in three dimensions will depend on microtubule orientation, and the detection bandpass filter used here will have to be replaced by more sophisticated, orientation invariant methods. However, full three-dimensional analysis will also require faster acquisition at sufficient temporal and axial resolution, and development of brighter, more photostable fluorescent probes. However, the ease of EB1-EGFP imaging makes our method attractive for high-content screening applications, in which microtubule dynamics may be relevant indicators of cell state.

METHODS

Methods and any associated references are available in the online version of the paper at http://www.nature.com/naturemethods/.

Note: Supplementary information is available on the Nature Methods website.

AUTHOR CONTRIBUTIONS
A.M. designed and implemented algorithms for comet detection and track clustering, and performed computer vision and statistical analysis. P.K. and T.W. acquired EB1-EGFP and mCherry-tubulin datasets. C.T. and W.K. generated data for the comparison of EB3-EGFP and CLIP170-EGFP comet dynamics in pVHL knockdown cells.

1. Desai, A. & Mitchison, T.J. Microtubule polymerization dynamics. *Annu. Rev. Cell Dev. Biol.* **13**, 83–117 (1997).
2. Sammak, P.J. & Borisy, G.G. Direct obsrevation of microtubule dynamics in living cells. *Nature* **332**, 724–726 (1988).
3. Rusan, N.M., Fagerstrom, C.J., Yvon, A.M.C. & Wadsworth, P. Cell cycle-dependent changes in microtubule dynamics in living cells expressing green fluorescent protein-alpha tubulin. *Mol. Biol. Cell* **12**, 971–980 (2001).
4. Wittmann, T., Bokoch, G.M. & Waterman-Storer, C.M. Regulation of leading edge microtubule and actin dynamics downstream of Rac1. *J. Cell Biol.* **161**, 845–851 (2003).
5. Altinok, A. *et al.* Model based dynamics analysis in live cell microtubule images. *BMC Cell Biol.* **8** (Suppl. 1), S4 (2007).
6. Waterman-Storer, C.M. & Salmon, E.D. How microtubules get fluorescent speckles. *Biophys. J.* **75**, 2059–2069 (1998).
7. Salmon, W.C., Adams, M.C. & Waterman-Storer, C.M. Dual-wavelength fluorescent speckle microscopy reveals coupling of microtubule and actin movements in migrating cells. *J. Cell Biol.* **158**, 31–37 (2002).
8. Akhmanova, A. & Steinmetz, M.O. Tracking the ends: a dynamic protein network controls the fate of microtubule tips. *Nat. Rev. Mol. Cell Biol.* **9**, 309–322 (2008).
9. Salaycik, K.J., Fagerstrom, C.J., Murthy, K., Tulu, U.S. & Wadsworth, P. Quantification of microtubule nucleation, growth and dynamics in wound-edge cells. *J. Cell Sci.* **118**, 4113–4122 (2005).
10. Bieling, P. *et al.* CLIP-170 tracks growing microtubule ends by dynamically recognizing composite EB1/tubulin-binding sites. *J. Cell Biol.* **183**, 1223–1233 (2008).
11. Dragestein, K.A. *et al.* Dynamic behavior of GFP-CLIP-170 reveals fast protein turnover on microtubule plus ends. *J. Cell Biol.* **180**, 729–737 (2008).
12. Rosin, P.L. Unimodal thresholding. *Pattern Recognit.* **34**, 2083–2096 (2001).
13. Yang, G., Matov, A. & Danuser, G. Reliable tracking of large-scale dense particle motion for fluorescent live cell imaging. *IEEE Int. Conf. Comp. Vis. Patt. Rec.* **3**, 138 (2005).
14. Verde, F., Dogterom, M., Stelzer, E., Karsenti, E. & Leibler, S. Control of microtunbule dynamics and length by cyclin A-dependent and cyclin B-dependent kinases in *Xenopus* egg extracts. *J. Cell Biol.* **118**, 1097–1108 (1992).
15. Hawkins, T., Mirigian, M., Yasar, M.S. & Ross, J.L. Mechanics of microtubules. *J. Biomech.* **43**, 23–30 (2010).
16. Brangwynne, C.P., MacKintosh, F.C. & Weitz, D.A. Force fluctuations and polymerization dynamics of intracellular microtubules. *Proc. Natl. Acad. Sci. USA* **104**, 16128–16133 (2007).
17. Schrijver, A. *Combinatorial Optimization*. (Springer, Heidelberg, 2003).
18. Jaqaman, K. *et al.* Robust single-particle tracking in live-cell time-lapse sequences. *Nat. Methods* **5**, 695–702 (2008).
19. Vasquez, R.J., Howell, B., Yvon, A.M.C., Wadsworth, P. & Cassimeris, L. Nanomolar concentrations of nocodazole alter microtubule dynamic instability in vivo and in vitro. *Mol. Biol. Cell* **8**, 973–985 (1997).
20. Yvon, A.M.C., Wadsworth, P. & Jordan, M.A. Taxol suppresses dynamics of individual microtubules in living human tumor cells. *Mol. Biol. Cell* **10**, 947–959 (1999).
21. Hammond, J.W., Cai, D.W. & Verhey, K.J. Tubulin modifications and their cellular functions. *Curr. Opin. Cell Biol.* **20**, 71–76 (2008).
22. Hubbert, C. *et al.* HDAC6 is a microtubule-associated deacetylase. *Nature* **417**, 455–458 (2002).
23. Komarova, Y.A., Vorobjev, I.A. & Borisy, G.G. Life cycle of MTs: persistent growth in the cell interior, asymmetric transition frequencies and effects of the cell boundary. *J. Cell Sci.* **115**, 3527–3539 (2002).
24. Kumar, P. *et al.* GSK3 beta phosphorylation modulates CLASP-microtubule association and lamella microtubule attachment. *J. Cell Biol.* **184**, 895–908 (2009).
25. Mimori-Kiyosue, Y. *et al.* CLASP1 and CLASP2 bind to EB1 and regulate microtubule plus-end dynamics at the cell cortex. *J. Cell Biol.* **168**, 141–153 (2005).
26. Vitre, B. *et al.* EB1 regulates microtubule dynamics and tubulin sheet closure *in vitro*. *Nat. Cell Biol.* **10**, 415–421 (2008).
27. Komarova, Y. *et al.* Mammalian end binding proteins control persistent microtubule growth. *J. Cell Biol.* **184**, 691–706 (2009).
28. Skube, S.B., Chaverri, J.M., & Goodson, H.V. Effect of GFP tags on the localization of EB1 and EB1 fragments *in vivo*. *Cytoskeleton* **67**, 1–12 (2010).
29. Honnappa, S. *et al.* An EB1-binding motif acts as a microtubule tip localization signal. *Cell* **138**, 366–376 (2009).
30. Jaqaman, K. *et al.* Kinetochore alignment within the metaphase plate is regulated by centromere stiffness and microtubule depolymerases. *J. Cell Biol.* **188**, 665–679 (2010).

ONLINE METHODS

Software. The ClusterTrack software is available as **Supplementary Software 1** and at http://lccb.hms.harvard.edu/software.html; a user-friendly software package with additional functionality for track visualization and statistical processing, not described here, is available at the same website.

Cell culture and microscopy. HaCaT keratinocytes stably expressing EB1-EGFP were grown in DMEM with 10% FBS and 250 μg ml^{-1} geneticin at 37 °C and 5% CO_2. Sequence encoding mCherry-tagged tubulin was introduced into cells by infection with a recombinant adenovirus. Cells were treated with nocodazole, taxol or trichostatin A for ~60 min before imaging. For microscopy, cells were grown on #1.5 coverslips, and the medium was supplemented with 10 mM K-HEPES (pH 7.0). Cells were imaged at 37 °C with a 100× numerical aperture (NA) 1.49 or a 60× NA 1.45 objective lens (CFI APO TIRF; Nikon) on an inverted microscope system (TE2000 Perfect Focus System; Nikon) equipped with a spinning-disk confocal unit (CSU10; Yokogawa) with 200 mW, 488 nm and 561 nm solid-state lasers (LMM5; Spectral Applied Research), electronic shutters, a cooled charge-coupled device camera (Cool-SNAP HQ2; Photometrics) and controlled by NIS-Elements software (Nikon).

Image analysis. All programs for EB1-EGFP comet detection, tracking and geometrical clustering were written in Matlab (Mathworks) and C++. Hand-tracking of microtubule ends in the dual-wavelength validation movie was done using the tracking function in NIS-Elements. Movies were generated with MetaMorph (Molecular Dynamics) and QuickTime Pro (Apple).

Statistical comparison of parameters of microtubule dynamics. None of the parameters of microtubule dynamics (rates of growth and shrinkage, duration of growth, shrinkage and pauses) were normally distributed. To determine the significance of differences in the mean values between parameters under different experimental conditions, we applied a permutation t-test. In brief, for specific parameters 400 values were bootstrap-sampled from the data of different experimental conditions. In agreement with the central limit-theorem, the two distributions of the means were always normal and thus could be analyzed for differences using regular Student t-test statistics.